Journal of Materials Chemistry A

ROYAL SOCIETY OF CHEMISTRY

COMMUNICATION

View Article Online
View Journal | View Issue

Cite this: J. Mater. Chem. A, 2025, 13, 1766

Received 8th November 2024
Accepted 16th December 2024

DOI: 10.1039/d4ta07954j

rsc.li/materials-a

High-conductivity, low-temperature sintering-compatible NASICON solid electrolyte for enhanced compositing with hard carbon electrode in all-solid-state batteries†

Bowei Xun, [a] Jian Wang, [a] Yukio Sato, [b] George Hasegawa, [c] Hirofumi Akamatsu [a] and Katsuro Hayashi *[a]

Oxide-based all-solid-state sodium-ion batteries present a safer, more robust and more sustainable alternative to lithium-ion batteries, though fabrication challenges persist, particularly during co-sintering. In this study, we demonstrate that by adding sodium borate-based sintering aids to highly conductive $Na_3Zr_2(SiO_4)_2(PO_4)$ (NZSP)-based materials, both a lower sintering temperature and high ionic conductivity can be achieved. Specifically, the mixture of Na_2CO_3 and B_2O_3 as a sintering aid is crucial, and samples sintered at 900 °C with a $Na_{3.4}Zr_{1.95}Al_{0.05}(SiO_4)_{2.35}(PO_4)_{0.65}$ composition exhibits a Na^+ ion conductivity exceeding 4×10^{-3} S cm^{-1} at room temperature. These materials are also compatible with co-sintering alongside hard carbon anode materials. The all-solid-state cell, featuring a composite electrode of spherical hard carbon particles and optimized NZSP-based electrolytes, demonstrated stable charge–discharge performance at room temperature, retaining a capacity of 140–220 mA h g^{-1} across 80 cycles.

Oxide-based all-solid-state sodium-ion batteries (Na ASSBs) are regarded as a safer, more robust, and more sustainable alternative to traditional lithium-ion batteries (LIBs). However, challenges persist in their fabrication, particularly in the co-sintering of materials such as electrolytes, electrode active materials, and other components.[1–3] NASICON-type $Na_3Zr_2(SiO_4)_2(PO_4)$ (NZSP)-based materials are promising candidates for solid electrolytes due to their high ionic conductivity and moderate sintering temperatures. Through various chemical modifications, the ionic conductivity of NZSP-based electrolytes, which are sintered at around 1250 °C, can reach levels comparable to sulfide-based electrolytes.[4–7] (For summary of reported data, see ESI Table S1.†) Recently, we demonstrated that optimizing the Si/P ratio and introducing a small amount

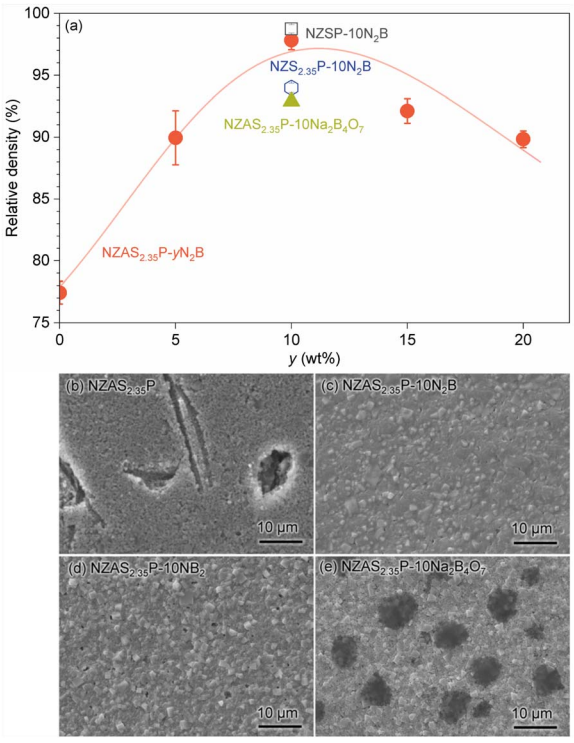

Fig. 1 Sinterability and microstructure of NZSP-based electrolytes sintered at 900 °C for 12 h in air. (a) The relative density of the NZSP, $NZS_{2.35}P$, and $NZAS_{2.35}P$ ceramics, as the function of the wt% of $2Na_2CO_3 + B_2O_3$ (N_2B) additive, and $NZAS_{2.35}P$-10$Na_2B_4O_7$. The relative density is based on the theoretical value (3.27 g cm^{-3}) for NZSP for simplicity. (b–e) Surface SEM images for $NZAS_{2.35}P$ (b) without the sintering aid (average grain size of <0.3 μm), (c) with 10 wt% N_2B (0.7 μm), (d) with 10 wt% NB_2(0.6 μm), and (e) with 10 wt% $Na_2B_4O_7$ (0.5 μm).

[a]Department of Applied Chemistry, Graduate School of Engineering, Kyushu University, 744 Motooka, Nishi-ku, Fukuoka 819-0395, Japan. E-mail: k.hayashi@cstf.kyushu-u.ac.jp

[b]Research and Education Institute for Semiconductors, Informatics, Kumamoto University, 2-39-1 Kurokami, Chuo-ku, Kumamoto 860-8555, Japan

[c]Institute of Materials and Systems for Sustainability, Nagoya University, Furo-cho, Chikusa-ku, Nagoya 464-8601, Japan

† Electronic supplementary information (ESI) available: Detailed experimental methods; summary of literature about NZSP-based ceramics with sintering-aid; XRD; Rietveld analysis; particle size in sinters; DC polarization measurement; charge–discharge curves of HCS electrode in a liquid electrolyte cell; Scotch tape test; STEM-EDS analysis; EIS. See DOI: https://doi.org/10.1039/d4ta07954j

of Al dopant resulted in a record conductivity of 6×10^{-3} S cm^{-1} at room temperature (RT).[8]

To address the need for lower sintering temperatures, liquid-phase sintering aids have been investigated.[9–17] For example, Na_3BO_3 can lower sintering temperatures to 700–900 °C (ref. 10 and 14) while maintaining an RT conductivity more than 1×10^{-3} S cm^{-1} for a material sintered at 900 °C.[14] (For sintering temperature-conductivity trend, see ESI Fig. S1.†) This study focuses on further enhancing the conductivity by employing the chemically-modified NZSPs combined with sodium borate-based sintering aids. Our findings show that a total conductivity of $>4 \times 10^{-3}$ S cm^{-1} at RT is achievable at a reduced sintering temperature of 900 °C using the optimal chemical composition and preparation method.

The study also incorporates hard carbon (HC) as an electrode active material in a composite electrode for Na ASSBs, highlighting the compatibility of high-conductivity, low-sintering-temperature materials. HCs, or non-graphitizing carbons, are widely recognized as suitable sodium-insertion negative electrode materials for liquid-electrolyte-based sodium-ion batteries.[18–21] Well-engineered HCs can deliver even higher electrochemical capacities[21,22] than the theoretical value for lithium in graphite insertion compound (Li-GIC, 372 mA h g^{-1}),[23] with a smaller volume expansion upon full insertion/deinsertion (13.2% for C to LiC_6).[24] The latter property may be particularly beneficial for ASSB systems, which often consists of materials with lower mechanical compliance.[25] However, despite the potential of HCs, their integration *via* sintering has not been extensively explored, likely due to the challenging reactivity between oxide and carbon materials. This study successfully demonstrates the compositing of NZSP-based electrolytes with HC through atmospheric pressure sintering at

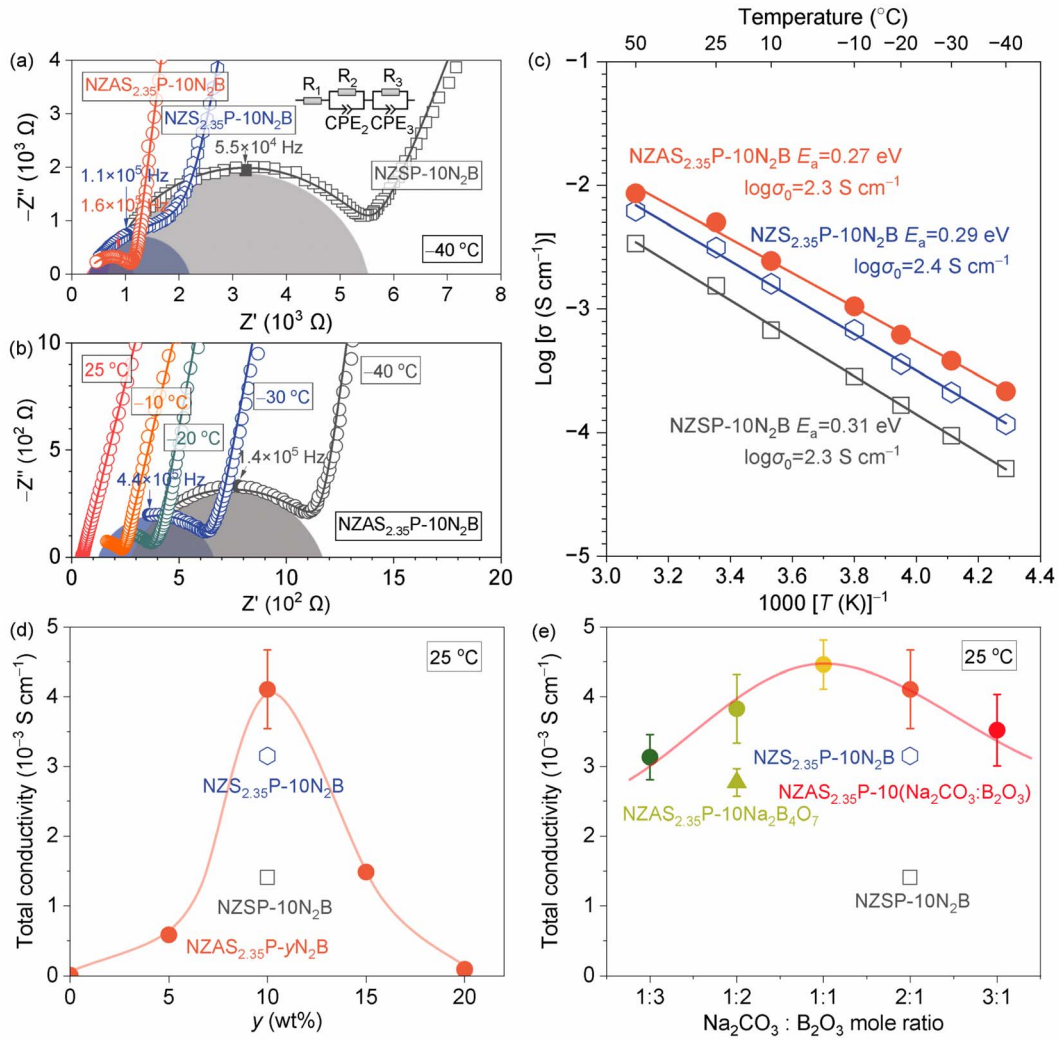

Fig. 2 Ionic conductivity measured by EIS. (a) Nyquist plots for NZSP-10N_2B (black), NZ$S_{2.35}$P-10N_2B (blue), and NZ$AS_{2.35}$P-10N_2B (red) at −40 °C (open symbols), with fitting curves (solid lines) by equivalent circuit modeling (inset). The semicircles corresponding to the grain boundary (parallel R_2-CPE_2) components are shaded. (b) Nyquist plots of the total conductivity measured for NZ$AS_{2.35}$P-10N_2B at temperatures ranging from −40 to 25 °C. (c) Arrhenius plots of the total conductivities at temperatures ranging from −40 to 50 °C for the samples in (a). (d) Total conductivity of NZSP-10N_2B, NZ$S_{2.35}$P-10N_2B, and NZ$AS_{2.35}$P-$y$$N_2$B ($y$ = 0–20) at 25 °C (e) total conductivity of NZSP-10N_2B (open square), NZ$S_{2.35}$P-10N_2B (open hexagon), NZ$AS_{2.35}$P added with different ratios of Na_2CO_3 and B_2O_3 from N_3B to NB_3 (filled circles), and NZ$AS_{2.35}$P added with $Na_2B_2O_7$ (filled triangle) at 25 °C.

900 °C, achieving good electrochemical performance at RT without the need for organic or liquid agents.

In our previous study,[8] ceramic samples with the compositions $Na_3Zr_2(SiO_4)_2(PO_4)$ (NZSP), $Na_{3.35}Zr_2(SiO_4)_{2.35}(PO_4)_{0.65}$ ($NZS_{2.35}P$), and $Na_{3.4}Zr_{1.95}Al_{0.05}(SiO_4)_{2.35}(PO_4)_{0.65}$ ($NZAS_{2.35}P$) were prepared by sintering at 1270 °C in air. Among these, the Al-doped $NZAS_{2.35}P$ exhibited the highest ionic conductivity. In this study, a 10 wt% mixture of Na_2CO_3 and B_2O_3 in a 2 : 1 molar ratio (abbreviated as $10N_2B$) was added into the three base compositions, and dense ceramics were obtained by sintering at 900 °C for 12 h in air. Additionally, $NZAS_{2.35}P$ samples with varying amounts (y wt%) of N_2B, ranging from 0 to 20 wt% ($NZAS_{2.35}P$-yN_2B), as well as samples containing 10 wt% $Na_2B_4O_7$ ($NZAS_{2.35}P$-$10Na_2B_4O_7$), were prepared for comparison. X-ray diffractometry (XRD) confirmed that these samples predominantly consist of NASICON-type crystals with a monoclinic space group $C2/c$, along with minor secondary phases of ZrO_2 (ESI Fig. S2†). Rietveld analysis was performed on the XRD patterns of NZSP-$10N_2B$ and $NZAS_{2.35}P$-$10N_2B$ (ESI Fig. S3, Tables S2 and S3†), confirming that crystallographic features of NASICON phases inherit those of NZSP and $NZAS_{2.35}P$ in our previous study.[8] The amount of ZrO_2 in these samples was typically ~5%.

Fig. 1 presents the relative densities of the samples, along with scanning electron microscopy (SEM) images of the sintered surfaces for selected samples. The relative density peaks at y = 10 wt%, indicating that this is the optimal additive amount for densification. The composition of the NZSP-based materials has a minor impact on densification. Without the use of sintering aids (Fig. 1b), numerous voids are present, and crystal growth is limited. The samples with sintering aids (Fig. 1c–e) show well-densified microstructures with enhanced grain growth and very few pores (average grain size data, see ESI Fig. S4†). There is a distinct difference in microstructure between those with Na_2CO_3 and B_2O_3 added separately (Fig. 1c and d) and that with $Na_2B_4O_7$ added directly (Fig. 1e). The former samples exhibit a macroscopically uniform appearance, while the latter display dark-contrast aggregates, suggesting they are amorphous aggregates composed of lighter elements. These aggregates are enriched with the $Na_2B_4O_7$ component, indicating poor wetting with the host crystalline phase. In the case of the separate NB_2 addition, CO_2 is expected to be released during sintering, resulting in a composition similar to $Na_2B_4O_7$; however, the microstructure differs significantly. This suggests that the separate addition and *in situ* reaction are significant for enhancing wetting properties.

Electrical conductivity in the prepared samples was measured using electrochemical impedance spectroscopy (EIS). Nyquist plots for NZSP-$10N_2B$, $NZS_{2.35}P$-$10N_2B$, and $NZAS_{2.35}P$-$10N_2B$ at −40 °C were fitted by an equivalent circuit model, identifying bulk and grain boundary resistances (Fig. 2a). Notably, the grain boundary resistance in $NZAS_{2.35}P$-$10N_2B$ decreased with increasing temperature, becoming negligible at 25 °C (Fig. 2b). DC polarization measurements at 25 °C (ESI Fig. S5†) revealed very low partial electronic conductivities. For instance, the electronic conductivity in $NZAS_{2.35}P$-$10N_2B$ was approximately five orders of magnitude lower than the total conductivity, confirming its pure Na^+ ion conducting nature.

The conductivity (σ)–temperature (T) relationship followed Arrhenius behavior with activation energies (E_a) ranging from 0.27 to 0.31 eV (Fig. 2c). The value of E_a and the pre-exponential factor (σ_0) indicated in the figure were estimated from the equation $\sigma T = \sigma_0 \exp(-E_a/k_B T)$, where k_B is the Boltzmann constant. $NZAS_{2.35}P$-based samples with varying N_2B content exhibited a peak conductivity of 4.1×10^{-3} S cm^{-1} at 10 wt% N_2B (Fig. 2d), while conductivity significantly dropped to 4.2 ×

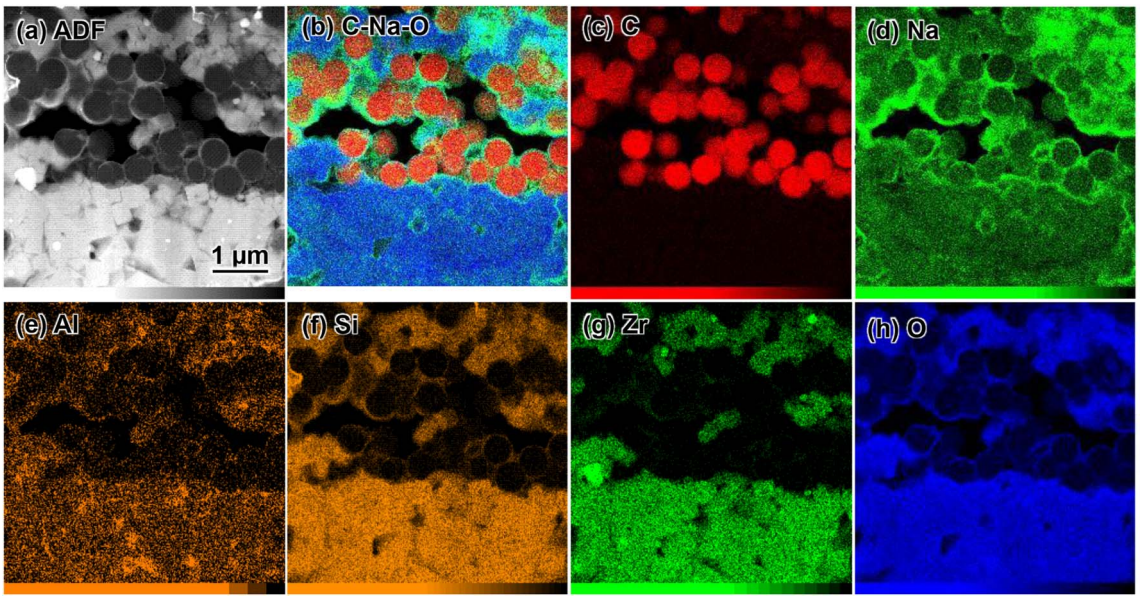

Fig. 3 STEM analyses for the cross section of HCS-$NAS_{2.35}P$-$10N_2B$ composite electrode (upper side) on $NAS_{2.35}P$-$10N_2B$ ceramic substrate (lower side). (a) High-angle annular dark-field (HAADF) image; and (b–h) elemental distribution maps obtained by EDS for (b) composite of C (red), Na (green) and O (blue), (c) C, (d) Na, (e) Al, (f) Zr, (g) Zr, and (h) O K-line signals.

10^{-6} S cm^{-1} without the sintering aid. All $NZAS_{2.35}P$-based samples containing 10 wt% of additives with different Na_2CO_3 and B_2O_3 ratios showed improved conductivity, with a maximum value of 4.5×10^{-3} S cm^{-1} for the 1 : 1 ratio (Fig. 2e). It is noted that the conductivity in $NZAS_{2.35}P$-$10Na_2B_4O_7$ was lower than that of $NZAS_{2.35}P$-$10NB_2$. Thus, a homogeneous microstructure as well as grain growth are essential for reducing grain boundary resistivity. Additionally, the base chemical composition also plays a decisive role in conductivity, impacting both bulk and grain boundary properties as discussed in our previous paper.[8]

A spherical-shaped hard carbon (hard carbon sphere, HCS) powder with particle sizes ranging from 0.4 to 0.6 μm was prepared from a hydrothermally synthesized resorcinol-formaldehyde (RF)-gel precursor, followed by a calcination in an N_2 atmosphere.[26] This electrode material delivered 272 mA h g^{-1} at room temperature and at the rate of 100 mA g^{-1} in a liquid electrolyte cell (ESI Fig. S6†). The HCS powder is investigated as a potential negative electrode material for in an ASSB. A composite electrode layer, consisting of HCS and $NZAS_{2.35}P$-$10N_2B$ with weight ratio of 3 : 4, corresponding to a volume ratio of approximately 6 : 5, was formed by spin coating onto an $NZAS_{2.35}P$-$10N_2B$ ceramic substrate and subsequently heated at 900 °C in an N_2 atmosphere to consolidate the coating layer. After sintering, the thick film was mechanically strong enough to adhere to the electrolyte substrate (ESI Fig. S7†). Preservation of the NASICON phase was confirmed by XRD (ESI Fig. S2†).

Fig. 3 presents the scanning transmission electron microscopy (STEM) and energy-dispersive X-ray spectroscopy (EDS) analysis of cross-section of HCS-$NZAS_{2.35}P$-$10N_2B$|$NZAS_{2.35}P$-$10N_2B$ junction. The composite electrode layer, approximately 4–5 μm in thickness, exhibit a partially aggregated distribution of HCS with NZSP-based electrolyte and voids. The interfacial regions are well densified, forming close and intimate junctions. Areas with electrolyte particle aggregation are also densified, while voids are observed in regions lacking sufficient electrolyte, supporting that the $NZAS_{2.35}P$-$10N_2B$ components serve as a 'binder' for the HCS.

The EDS maps (Fig. 3b–h) reveal that the region surrounding HCS enriched with Na and O components. This material appears to have excellent wettability with the HCS and is likely attributed to the solidified sodium borate-based phase, where B atoms are undetectable by EDS. Closer observation reveals that the interfacial layer surrounding the HCS contains not only Si and Al but also Zr, although P could not be sufficiently distinguished from Zr by EDS (ESI Fig. S8†). This suggests a process involving the dissolution and precipitation of $NZAS_{2.35}P$ components *via* a liquid phase during sintering. In contrast, Al is preferentially segregated at the grain boundaries and triple junctions of the $NZAS_{2.35}P$ crystals, giving these regions a different chemical identity from the that around the HCS (ESI Fig. S8†). This leads to the assumption that, as the sintering progresses, the residual sodium borate-based liquid phase are expelled from the electrolyte region and accumulated around the HCS. Resultant Na-rich interfacial layer is expected to mediate Na diffusion during battery operation.

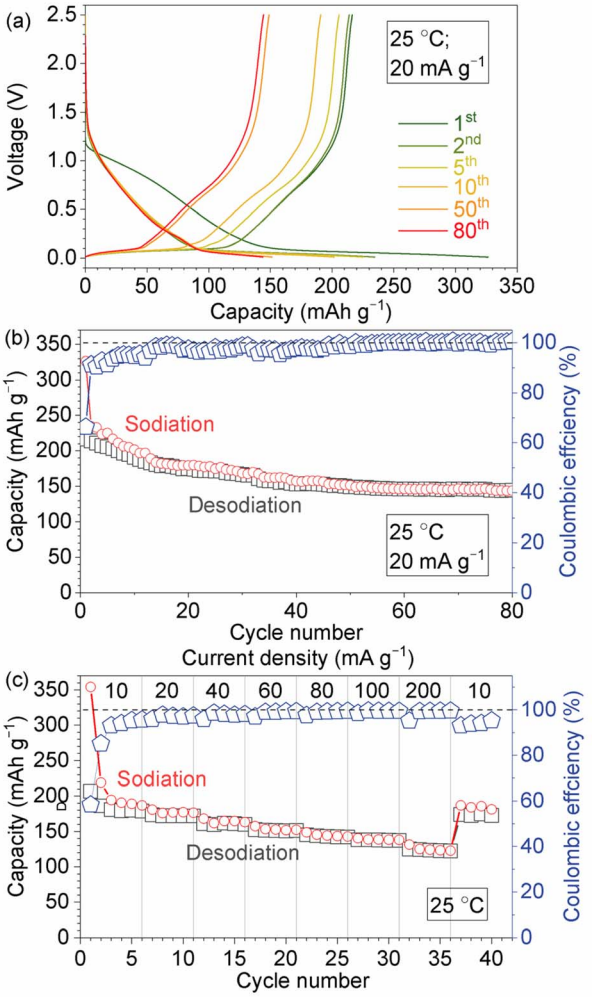

Fig. 4 Electrochemical properties in a half cell of Na|$NZAS_{2.35}P$-$10N_2B$|HCS-$NZAS_{2.35}P$-$10N_2B$ composite electrode at 25 °C. (a) Charge–discharge curves of selected cycles measured at a current density of 6 μA cm^{-2}, corresponding to 20 mA g^{-1}, in cut-off voltage ranges from 0.01 to 2.5 V; (b) electrochemical capacities and coulombic efficiency for discharge cycles; (c) rate performances and coulombic efficiency at various current densities ranging from 10 to 200 mA g^{-1}.

The electrochemical properties of the composite electrode formed on the electrolyte substrate were investigated in a half-cell configuration with a metallic Na counter electrode. Fig. 4a presents the charge and discharge curves measured at a current density of 20 mA g^{-1}. The curves exhibit a characteristic sloping region above ~0.1 V and plateau region between 0.01 and 0.1 V, similar to those observed in liquid electrolyte systems.[20,22,23,27] The first sodiation and desodiation capacities are 330 and 220 mA h g^{-1}, respectively, based on the weight of HCS, with an initial coulombic efficiency of 66%. The observed irreversibility during the initial cycles in the solid-state system remains a topic for future investigation. In subsequent cycles, the discharge capacity gradually decreases to 140 mA h g^{-1}, while the coulombic efficiency improves to over 99% (Fig. 4b). The EIS before and after 80 cycles showed no significant changes in

resistance associated with the electrolyte–electrode interface, and the low-frequency response, related to diffusion in the composite electrode, exhibited a small decrease in capacitance and resistance, likely relating to the change in electrochemical properties of HCSs (ESI Fig. S9†). Fig. 4c shows the results of rate-dependent capacity measurements, the cell delivers 140 mA h g^{-1} at a high current density of 200 mA g^{-1}. When the current density is reduced back to 10 mA g^{-1}, the cell recovers a capacity of 180 mA h g^{-1}, overall substantiating stable interface formation and efficient Na^+ ion transport between the composite electrode and the electrolyte.

Conclusions

In summary, we demonstrated that the addition of (optimally 10 wt%) mixture of Na_2CO_3 and B_2O_3 to NASICON-based materials may produce highly conductive Na^+ ion solid electrolyte, achieving a maximum conductivity of 4.5×10^{-3} S cm^{-1} at 25 °C, with a reduced sintering temperature of 900 °C. A composite electrode, consisting of hard carbon spheres (HCS) and $NZAS_{2.35}P\text{-}10N_2B$, was fabricated by consolidating the mixture through heating at 900 °C in an N_2 atmosphere. Electrochemical testing revealed initial charge and discharge capacities of 330 and 220 mA h g^{-1}, respectively, followed by a gradual decrease in capacities to 140 mA h g^{-1} and improved coulombic efficiency over successive cycles. These results highlight the successful electrochemically active integration of HCS with a NZSP-based electrolyte without the need for organic or liquid additives, representing an advancement toward the development of oxide-based Na ASSB.

Data availability

The data supporting this article have been included as part of the ESI.† The datasets generated and/or analyzed during the current study are available from the corresponding author upon reasonable request.

Author contributions

B. Xun: preparation for materials, collecting data, investigation, formal analysis, writing original manuscript; J. Wang: investigation, review; Y. Sato: TEM analysis, review; G. Hasegawa: conceptualization, investigation, review; H. Akamatsu: review, funding acquisition; K. Hayashi: conceptualization, project administration, supervision, investigation, writing, review & editing, funding acquisition.

Conflicts of interest

The authors declare no competing financial interest.

Acknowledgements

This work was supported by Grant-in-Aid for Green Technologies of Excellence (GteX) (no. JPMJGX23S4) from Japan Science and Technology Agency (JST), Japan. The STEM analyses were carried out at Engineering Research Equipment Center, Kumamoto University. We thank Ziyue Zhang for experimental support. B. X. thanks the CSC scholarship sponsored by the China Scholarship Council (CSC).

References

1 G. Hasegawa and K. Hayashi, *APL Energy*, 2023, **1**, 020902.
2 D. Kutsuzawa, T. Kobayashi and S. Komiya, *ACS Appl. Energy Mater.*, 2022, **5**, 4025–4028.
3 D. Kutsuzawa and T. Kobayashi, *Batteries Supercaps.*, 2023, **6**, e202300075.
4 J. Yang, G. Liu, M. Avdeev, H. Wan, F. Han, L. Shen, Z. Zou, S. Shi, Y.-S. Hu and C. Wang, *ACS Energy Lett.*, 2020, **5**, 2835–2841.
5 Q. Ma, C.-L. Tsai, X.-K. Wei, M. Heggen, F. Tietz and J. T. S. Irvine, *J. Mater. Chem. A*, 2019, **7**, 7766–7776.
6 Y. B. Rao, K. K. Bharathi and L. N. Patro, *Solid State Ionics*, 2021, **366–367**, 115671.
7 S. Ohno, A. Banik, G. F. Dewald, M. A. Kraft, T. Krauskopf, N. Minafra, P. Till, M. Weiss and W. G. Zeier, *Prog. Energy*, 2020, **2**, 022001.
8 B. Xun, J. Wang, Y. Sato, S. Jia, S. Ohno, H. Akamatsu and K. Hayashi, *Adv. Energy Mater.*, 2024, 2402891.
9 H. Wang, G. Zhao, S. Wang, D. Liu, Z. Mei, Q. An, J. Jiang and H. Guo, *Nanoscale*, 2022, **14**, 823–832.
10 K. Suzuki, K. Noi, A. Hayashi and M. Tatsumisago, *Scr. Mater.*, 2018, **145**, 67–70.
11 Y. Zhao, C. Wang, Y. Dai and H. Jin, *Nano Energy*, 2021, **88**, 106293.
12 B. Santhoshkumar, M. B. Choudhary, A. K. Bera, S. M. Yusuf, M. Ghosh and B. Pahari, *J. Am. Ceram. Soc.*, 2022, **105**, 5011–5019.
13 J. A. S. Oh, L. He, A. Plewa, M. Morita, Y. Zhao, T. Sakamoto, X. Song, W. Zhai, K. Zeng and L. Lu, *ACS Appl. Mater. Interfaces*, 2019, **11**, 40125–40133.
14 K. Noi, K. Suzuki, N. Tanibata, A. Hayashi and M. Tatsumisago, *J. Am. Ceram. Soc.*, 2018, **101**, 1255–1265.
15 Y. Ji, T. Honma and T. Komatsu, *Materials*, 2021, **14**, 3790.
16 H. Wang, K. Okubo, M. Inada, G. Hasegawa, N. Enomoto and K. Hayashi, *Solid State Ionics*, 2018, **322**, 54–60.
17 K. Okubo, H. Wang, K. Hayashi, M. Inada, N. Enomoto, G. Hasegawa, T. Osawa and H. Takamura, *Electrochim. Acta*, 2018, **278**, 176–181.
18 M. Zhang, Y. Li, F. Wu, Y. Bai and C. Wu, *Nano Energy*, 2021, **82**, 105738.
19 B. Xiao, T. Rojo and X. Li, *ChemSusChem*, 2019, **12**, 133–144.
20 Y. Aniskevich, J. H. Yu, J.-Y. Kim, S. Komaba and S.-T. Myung, *Adv. Energy Mater.*, 2024, **14**, 2304300.
21 X. Dou, I. Hasa, D. Saurel, C. Vaalma, L. Wu, D. Buchholz, D. Bresser, S. Komaba and S. Passerini, *Mater. Today*, 2019, **23**, 87–104.
22 A. Kamiyama, K. Kubota, D. Igarashi, Y. Youn, Y. Tateyama, H. Ando, K. Gotoh and S. Komaba, *Angew. Chem., Int. Ed.*, 2021, **60**, 5114–5120.
23 S. Alvin, H. S. Cahyadi, J. Hwang, W. Chang, S. K. Kwak and J. Kim, *Adv. Energy Mater.*, 2020, **10**, 2000283.

24 S. Schweidler, L. de Biasi, A. Schiele, P. Hartmann, T. Brezesinski and J. Janek, *J. Phys. Chem. C*, 2018, **122**, 8829–8835.
25 J. A. S. Oh, G. Deysher, P. Ridley, Y.-T. Chen, D. Cheng, A. Cronk, S.-Y. Ham, D. H. S. Tan, J. Jang, L. H. B. Nguyen and Y. S. Meng, *Adv. Energy Mater.*, 2023, **13**, 2300776.
26 J. Liu, S. Z. Qiao, H. Liu, J. Chen, A. Orpe, D. Zhao and G. Q. (Max) Lu, *Angew. Chem., Int. Ed.*, 2011, **50**, 5947–5951.
27 Y. Morikawa, S. Nishimura, R. Hashimoto, M. Ohnuma and A. Yamada, *Adv. Energy Mater.*, 2020, **10**, 1903176.